Robustness of specimen design criteria for identification of anisotropic mechanical behaviour from heterogeneous mechanical fields

Jean-David Thoby, Thomas Fourest, Bertrand Langrand, Delphine Notta-Cuvier, Eric Markiewicz

Robustness of specimen design criteria for identification of anisotropic mechanical behaviour from heterogeneous mechanical fields

Jean-David Thoby[1,2], Thomas Fourest[1], Bertrand Langrand[1,2], Delphine Notta-Cuvier[2,3], and Eric Markiewicz[2]

[1]DMAS, ONERA, F-59014 Lille - France

[2]Univ. Polytechnique Hauts-de-France, CNRS, UMR 8201 - LAMIH, F-59313 Valenciennes, France

[3]INSA Hauts-de-France, F-59313 Valenciennes, France

Abstract

To reduce the number of tests required to characterise anisotropic elastoplastic constitutive models, an approach is to design specimen geometries to diversify the stress states generated in a single test. The experiments are then processed using an inverse identification method based on full-field measurements to achieve the full potential of that specific test. Recent optimization methods were able to design complex specimens in which highly heterogeneous stress fields were generated. However, the specimen design is only assessed based on numerical simulations and does not consider the effect of the biases introduced by the full-field measurement method. The goal of this work is therefore to take into account some of the most frequently observed measurement biases in the specimen selection process. The proposed approach uses synthetic test images generated with numerical simulations. Four specimen geometries have been ranked based on two selection criteria. The first one is an indicator of the heterogeneity of the stress fields obtained by finite element simulations (unbiased data). The second one quantifies error for the identification procedure due to measurement biases. The two criteria provide different rankings for the set of specimens. It is concluded that the design with the most heterogeneous stress fields (first criterion) is not necessarily the more robust design in terms of measurement noise (second criterion), so the optimized geometry should be selected based on a compromise between these two criteria.

1 Introduction

The commercial aviation industry constantly seeks to improve the efficiency of aircraft, which can potentially be achieved by using new lightweight materials for structural parts. Aircraft structure design is increasingly supported by numerical simulations of manufacturing techniques, part design and optimization. To ensure satisfactory predictions, these simulations particularly rely on the accurate modelling of material behaviour, which can be complex. For instance, the anisotropic behaviour of some laminated aluminum alloys, such as AA2198-T351, requires the use of an advanced anisotropic yield criterion [1]. 8 to 18 material parameters have to be determined for the use of the Barlat [2] or Bron and Besson criteria [3]. This large number of parameters is an advantage for the effective modelling of the behaviour of many materials. On the other hand, their identification might be costly.

Indeed, the first option for identifying the constitutive material parameters of this type of criterion is to perform numerous statically determined tests according to standards (NF EN ISO 6892). For laminated aluminum alloys, uniaxial tensile specimens are usually tested in three to seven loading directions with respect to the rolling direction. To better identify some criteria, additional shear or biaxial tensile tests are undertaken [4; 5]. Such statically determined approach requires spatially homogeneous stress during the tests. Each test provides the knowledge of a single stress state for the yield surface. An alternative approach is to use statically undetermined identification methods [6; 7; 8]. These methods may allow to take advantage of full-field measurement techniques and use local measurement data and therefore enrich measurements with heterogeneous mechanical fields. In this approach, a single test thus provides different stress states, which consequently reduces the number of required tests.

To robustly identify an anisotropic yield criterion, the test must generate diversified stress states to widely cover the yield surface. The ideal test should be able to generate local plasticity for combined biaxial and uniaxial tension, pure and simple shear, biaxial and uniaxial compression stresses. To achieve such heterogeneous stress states, several specimen geometries have been developed with different design approaches [9]. Specimen geometries can be defined empirically by adding simple geometric singularities like notches or holes to standard specimens adapted to uniaxial [10; 11; 12; 13; 14], biaxial [15; 16; 17] tensile machines and also bulge testing [18]. Other specimens were empirically designed from scratch by attempting to anticipate stress states in different locations on the specimen [12; 19]. The most recent approach is to use parametric [20; 21; 22] or topological [23; 24] optimization algorithms. A cost function is then required to run these optimizations. In the case of anisotropic yield criterion characterization, the cost function must quantify the

capacity of the specimen to generate heterogeneous stress fields [25; 26; 24]. However, the design methods developed rely exclusively on purely numerical data, *i.e.*, non-biased. Therefore, to the best of our knowledge, the robustness of an inverse identification procedure with full-field measurements using these specimens has not yet been evaluated.

The objective of the paper is to study the influence of biases when selecting a specimen for the identification of an anisotropic yield criterion. The paper focuses on the effects of experimental biases due to full-field measurements obtained with the Digital Image Correlation (DIC) method. More specifically, the biases studied are the effects of sensor noise, the speckle pattern and the edge reconstruction method. The biases are introduced using synthetic test images generated using an in-house algorithm [27]. Four specimens with increasing shape complexity will be ranked based on two selection criteria. The first one is an indicator of the heterogeneity of the stress fields obtained by finite element simulations. The second one quantifies the error in the identification procedure due to measurement biases. This paper is divided into two main sections. Firstly, the procedure for generating the synthetic test images and the different rankings are detailed in section 2. Then, the different rankings and the effects of measurement biases are analysed in section 3.

2 Synthetic test procedure

This section describes the material of interest, the specimens geometries and the two selection criteria.

2.1 Constitutive models for AA2198-T351

The material considered in this work is an aluminium-copper-lithium alloy AA2198-T351 laminated to a 4 mm thick sheet. This material is used in the aerospace industry to manufacture the main frame, the fuselage skin and aircraft webs. Elastic behaviour is modelled with the linear isotropic Hooke's law, which uses the following parameters: Young's modulus, E, and Poisson's ratio, ν. This material was tested by Chen et al. [1] for 6 mm thick sheets and they found that the Bron and Besson's criterion [3] was well suited for modelling the yield surface. With this criterion, the equivalent stress, σ_{eq}, is given as the sum of two equivalent stresses (Eq. 1), σ_{eq}^1 and σ_{eq}^2 (Eq. 2), weighted by the coefficient α. The exponents a, b^1 and b^2 control the global shape as with the Hosford isotropic criterion [28]. The anisotropy of the yield surface is controlled by the coefficients c_j^k used for the linear transformation of the stress tensor (Eq. 3). The limit of

the elastic domain is reached when $\sigma_{eq} = \sigma_y$ where σ_y is the yield stress (Eq. 4).

$$\left(\alpha \left(\sigma_{eq}^1\right)^a + (1-\alpha)\left(\sigma_{eq}^2\right)^a\right)^{1/a} = \sigma_{eq} \tag{1}$$

$$\begin{aligned} \sigma_{eq}^1 &= \left[\frac{1}{2}\left(|\tilde{S}_2^1 - \tilde{S}_3^1|^{b^1} + |\tilde{S}_3^1 - \tilde{S}_1^1|^{b^1} + |\tilde{S}_1^1 - \tilde{S}_2^1|^{b^1}\right)\right]^{1/b^1} \\ \sigma_{eq}^2 &= \left[\frac{3^{b^2}}{2^{b^2}+2}\left(|\tilde{S}_1^2|^{b^2} + |\tilde{S}_2^2|^{b^2} + |\tilde{S}_3^2|^{b^2}\right)\right]^{1/b^2} \end{aligned} \tag{2}$$

where $\tilde{S}_1^k$, $\tilde{S}_2^k$ and $\tilde{S}_3^k$ are the eigenvalues of $\tilde{\tilde{S}}^k$ (Eq. 3) with $k \in \{1, 2\}$.

$$\tilde{\tilde{S}}^k = \frac{1}{3}\begin{bmatrix} c_2^k + c_3^k & -c_3^k & -c_2^k & 0 & 0 & 0 \\ -c_3^k & c_3^k + c_1^k & -c_1^k & 0 & 0 & 0 \\ -c_2^k & -c_1^k & (c_1^k + c_2^k)/3 & 0 & 0 & 0 \\ 0 & 0 & 0 & 3c_4^k & 0 & 0 \\ 0 & 0 & 0 & 0 & 3c_1^5 & 0 \\ 0 & 0 & 0 & 0 & 0 & 3c_6^k \end{bmatrix} : \bar{\sigma} \tag{3}$$

The hardening behaviour is modelled as isotropic with a non-linear equation which is dependent on the cumulative plastic strain, ε^p. This hardening law has three constitutive material parameters: the initial yield stress, σ_0, the hardening modulus, K, and the hardening exponent, n (Eq. 4).

$$\sigma_y = \sigma_0 + K\left(1 - e^{-n\varepsilon^p}\right) \tag{4}$$

The parameters of the AA2198-T351 used in this work were identified in conventional tensile tests undertaken on seven specimen orientations with respect to the rolling direction. Tests were performed at least 3 times in each direction. First, the seven orientations were used to identify the parameters of the strain hardening model. Then the parameters of the Bron and Besson criterion were identified from the measurements of the elastic limits and the Lankford coefficients in all orientations. The Lankford coefficient is defined as $r = \varepsilon_{xx}^p / \varepsilon_{zz}^p$, where ε_{xx}^p and ε_{zz}^p are the plastic strain tensor components in the width and thickness directions, respectively. Their numerical values are reported in Table 1 and the stress-strain curves for three orientations are shown in Figure 1. In addition, the dependence of the initial yield stress and the Lankford coefficient on the test angle is shown in Figure 2. One can see that despite the large number of parameters used for the Bron and Besson model, variation in neither initial yield stress nor the Lankford coefficient can

be accurately modelled.

Table 1: Reference material parameters for the AA2198-T351

E [GPa]	ν [ ]	σ_0 [MPa]	K [MPa]	n [ ]
73.3	0.31	324.42	223.79	14.81
a [ ]	α [ ]	b^k [ ]		
19.9994	0.9989	a		
c_1^1 [ ]	c_2^1 [ ]	c_3^1 [ ]	c_4^1 [ ]	$c_{5,6}^1$ [ ]
1.2503	1.2622	0.5217	1.2453	1

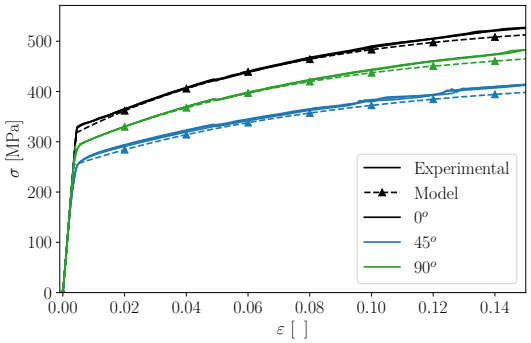

Figure 1: Experimental and numerical true stress-strain curves for the AA2198-T351. All experimental results are plotted.

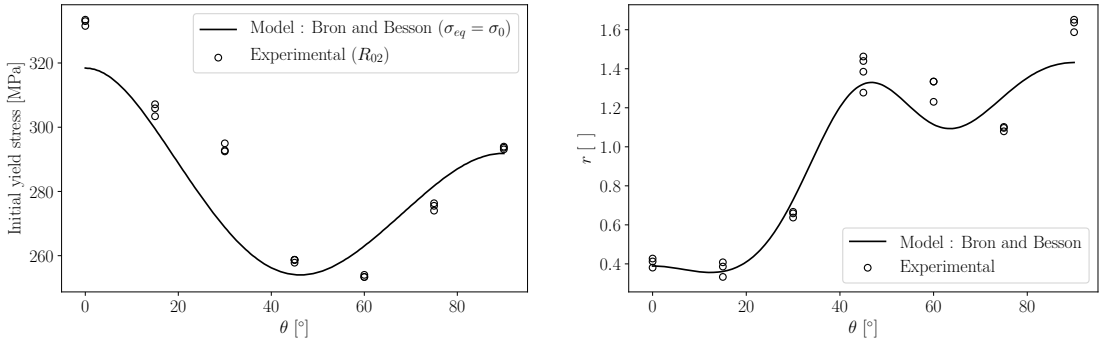

Figure 2: Experimental and numerical variations of the initial yield stress and the Lankford coefficient for the AA2198-T351 for uniaxial stress states with a angle, θ, of the rolling direction. All experimental results are plotted.

2.2 Selected specimen geometries

Four specimen geometries are considered in this work (Figure 3) with an increasing level of geometric complexity. The first geometry, referred to as "NOTCHED" is a simple notched specimen studied by Rossi *et*

al. [11]. Adding this simple geometric singularity should expand the stress states range away from uniaxial tension. The next two specimens were designed empirically by Kim *et al.* [12] and Jones *et al.* [19] and are referred to as "Σ" and "D" respectively. Both specimens generate more heterogeneous stress fields, and locally reach compression. Finally, a more complex specimen resulting from topological optimization by Barroqueiro *et al.* [23] was selected. This last specimen will be referred to as "OPTIMIZED". It generates a more heterogeneous stress field than the other three specimens. All geometries are considered to be machined at 45° with respect to the rolling direction of the sheet (associated with axis $\vec{1}$ on Figure 3). This orientation is chosen to enlarge the distribution of stress states in the $\vec{1}$ and $\vec{2}$ directions on the yield surface [11]. This set of specimens allows of different stress state heterogeneities to be investigated. More detailed information on the functional dimensions of the specimens can be found in their respective published papers.

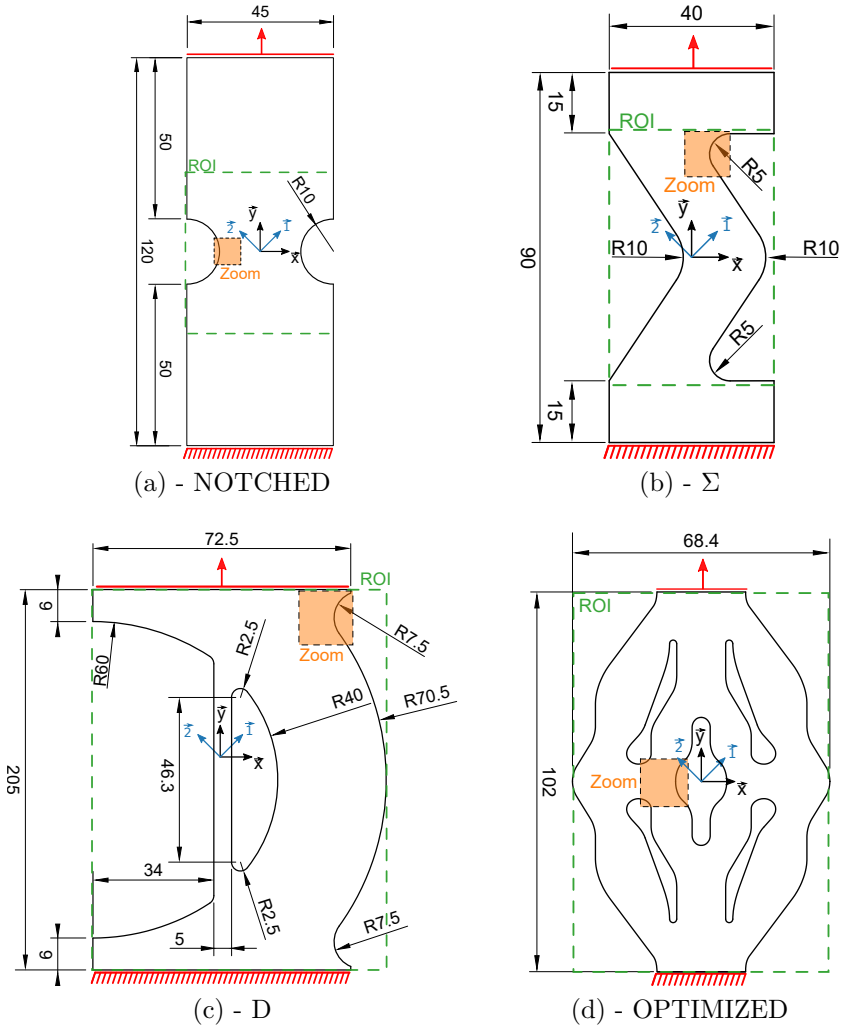

Figure 3: Dimensions of the four selected specimens and the associated boundary conditions and simulation frame ($\vec{x}$,$\vec{y}$) and material frame ($\vec{1}$,$\vec{2}$) for the FE simulation. All dimensions in mm.

2.3 Finite element models

Finite Element (FE) simulations are performed in order to provide an unbiased reference data-set to be used to calculate the heterogeneity indicator and to generate the synthetic images. These simulations were performed using the *Z-set* implicit solver to simulate tensile tests [29]. Linear triangular shell elements with full integration were used with the plane stress hypothesis in line with the surface measurement upon testing. The element size was equal to about 0.5 mm for all specimens. The mesh size was chosen after a convergence study. All degrees of freedom are blocked at the bottom edge whereas the displacement at the upper edge is blocked in direction $\vec{x}$ and imposed in direction $\vec{y}$. The material frame is oriented at 45° with respect to the loading frame (Figure 3). The simulations were stopped when the first element reached an equivalent plastic strain, ε^p, of 0.15. This limit has been arbitrarily set to exclude any damage mechanism (Figure 1) that would occur in real experiments.

2.4 Generating synthetic images

Synthetic test images were generated to evaluate the influence of the biases introduced by the full-field measurement method and sensor noise in the identification procedure. A speckle pattern is deformed based on the results of the previous FE simulations as in Bouda *et al.* [27]. For each pixel of coordinates (x_d, y_d) within an element, the corresponding isoparametric coordinates (ξ_i, η_i) are computed with the element shape functions. Then, the initial coordinates (x_0, y_0) of the corresponding point can be computed. Finally the grey level in the deformed configuration (x_d, y_d) is computed by linear interpolation of the grey level of neighbouring pixels in the reference configuration (Figure 4). To provide realistic texture images, speckle patterns were captured in experimental conditions. A Nikon D300 12M (4320×2868) sensor was used and a spray-painted texture was lit with two LED panels (appendix: Table A1). To include the sensor noise in the 201 synthetic test images, each synthetic test image is generated from a different image of the same texture. Therefore, a sequence of 201 images of the same undeformed pattern was recorded.

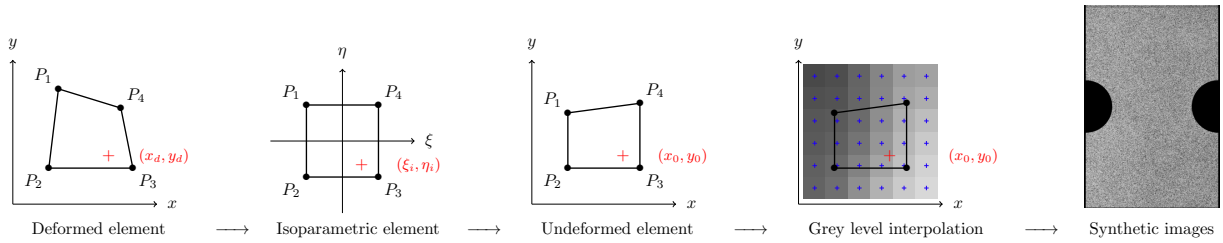

Figure 4: Schematic of the synthetic images generation process

To evaluate the influence of the speckle pattern in the following ranking method, two textures were painted and captured (Figure 5). The grey levels distribution is highly concentrated around 150 for speckle N°2, whereas speckle N°1 has two peaks at level 140 and 35 with a more uniform distribution of grey levels between these two peaks (Figure 6). The influence of the speckle pattern on measurement noise is investigated in the following section.

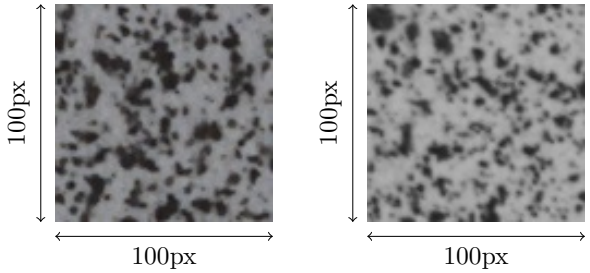

Figure 5: Sample of the speckle pattern captured

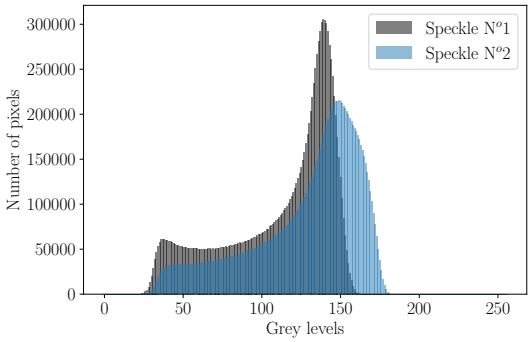

Figure 6: Grey level distribution for speckles

2.5 Digital image correlation

The Digital Image Correlation (DIC) method is used to compute the kinematic fields from the synthetic images. In this study, the FOLKI-D software developed by ONERA was used [30]. For each pixel, the in-plane strain fields (with small strain hypothesis) were computed using a first order polynomial fitting of the displacement field over a computation window. Then, the strain fields were spatially and temporally smoothed with Gaussian filters. Finally, data close to the edges were reconstructed by extending of the nearest value which is not corrupted by the invalid data close to the edges. Due to the complexity of each specimen, the DIC setup is independently defined for each specimen and each speckle pattern following the recommendation of the DIC Good Practices Guide [31]. The final configuration and the associated parame-

ters are reported in the appendices in Tables A2 and A3.

To evaluate the influence of the speckle pattern on the DIC measurement, the undeformed texture images were analysed to determine measurement noise. Figure 7 presents the typical noise error distribution for the three components of the strain tensor without regularisation. The noise error distributions show that in both cases the ε_{xx} and ε_{yy} components have similar noise levels and the ε_{xy} component is the least noisy as more data is concentrated close to zero. Although the grey level distribution with speckle pattern N°2 covers a wider range than N°1, when comparing the two speckles patterns, speckle pattern N°2 leads to more noise than N°1 in all strain components. The speckle feature size could be the reason for such a difference in noise level in the DIC measurement. Both textures are later used to study the influence of the pattern on the second selection criterion described below.

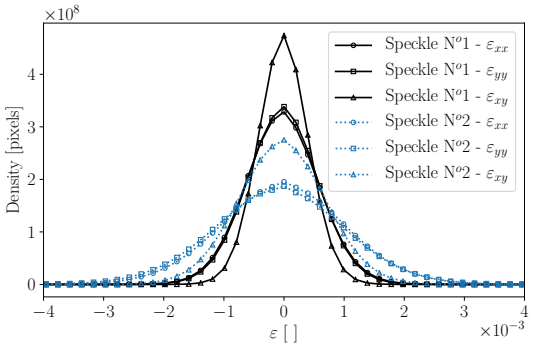

Figure 7: Typical noise error distribution computed using the DIC method in "static reference" (DIC subset size radius = 15pix)

2.6 First selection criterion: stress field heterogeneity

An indicator quantifies the performance of a novel geometry during the design process with a scalar value, thereby facilitating comparison and classification with respect to other geometries. Concerning the design of a specimen in order to identify an anisotropic yield surface, the performance of the tested geometry is related to the heterogeneity of the mechanical fields generated (strains or stresses). In this work, the heterogeneity indicator developed by Souto *et al.* is considered [26]. This indicator originally used the principal strain ratio ($\varepsilon_2/\varepsilon_1$) to characterize the strain states generated. In this work, this indicator is replaced by the triaxiality factor to analyse the stress states generated: $TF = (\sigma_H/\sigma_{eq})$ where σ_H is the hydro-static stress. The triaxiality factor is used aiming to analyse the distribution of the stress states on the yield surface. Indeed, the triaxiality factor can discriminate stress states between tension, shear and compression using a single

scalar value.

The modified indicator compromises two parts (Eq. 5). The first part expresses stress field heterogeneity through standard deviation for the triaxiality factor, $\mathrm{Std}\,(TF)$, and the range of the triaxiality factor, $(TF)_R$ (Eq. 6). The second part deals with the level of plastic strain reached in the specimen using standard deviation, $\mathrm{Std}\,(\varepsilon^p)$, the average value, $\mathrm{Av}_{\varepsilon^p}$, weighted by the volume of each element, V_i, and scaled by the volume of the ROI, V (Eq. 7) and the maximum value of plastic strain reached during the test, $\varepsilon^p_{\text{max test}}$. Finally, the stress state of each measurement point was classified into five categories (bi-tension, tension, shear, compression, bi-compression) with the respect of its TF value (Figure 8). The maximum value of plastic strain reached in each category was measured to define $\varepsilon^p_{\text{max}}$ (Eq. 8). Each term was calculated for all time steps and scaled with an absolute coefficient, w_{ai}, depending on its maximum value and weighted according to its attributed priority with relative coefficients, w_{ri}. More details about the original indicator and how to define the coefficient's values can be found in [26]. Table 2.6 summarizes the numerical values used in this work. Thus defined, the value of the indicator increases as the heterogeneity of the stress states generated in plastified areas increases.

$$I_T = \underbrace{w_{r1}\frac{\mathrm{Std}\,(TF)}{w_{a1}} + w_{r2}\frac{(TF)_R}{w_{a2}}}_{①} + \underbrace{w_{r3}\frac{\mathrm{Std}\,(\varepsilon^p)}{w_{a3}} + w_{r4}\frac{\varepsilon^p_{\text{max}}}{w_{a4}} + w_{r5}\frac{\mathrm{Av}_{\varepsilon^p}}{w_{a5}}}_{②} \tag{5}$$

$$(TF)_R = (TF)_{\text{max}} - (TF)_{\text{min}} \tag{6}$$

$$\mathrm{Av}_{\varepsilon^p} = \frac{\sum_{i=1}^{n} \varepsilon^p_i V_i}{V} \tag{7}$$

$$\varepsilon^p_{\text{max}} = \frac{\varepsilon^p_{\text{max. test}} + \varepsilon^p_{\text{max. tens.}} + \varepsilon^p_{\text{max. bi-tens.}} + \varepsilon^p_{\text{max. shear}} + \varepsilon^p_{\text{max. comp.}} + \varepsilon^p_{\text{max. bi-comp.}}}{6} \tag{8}$$

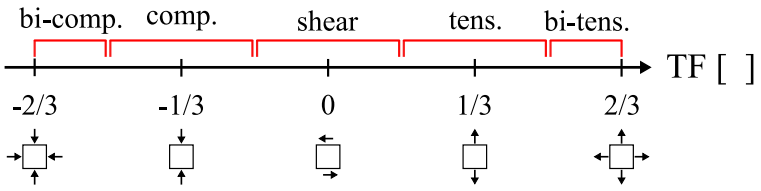

Figure 8: Triaxiality factors associated with specific stress states.

Table 2: Relative and absolute coefficient values of the indicator weighting coefficient.

w_{r1}	w_{r2}	w_{r3}	w_{r4}	w_{r5}
0.3	0.03	0.17	0.4	0.1
w_{a1}	w_{a2}	w_{a3}	w_{a4}	w_{a5}
2/3	4/3	0.25	0.15	0.15

2.7 Second selection criterion : the Virtual Fields Method

The original heterogeneity indicator (used for the first selection criterion) was developed to optimize specimens using unbiased data. Therefore, calculating its value using biased data may not reflect the robustness of the final identification problem to biases. In this work, we propose using the Virtual Fields Method (VFM) for biased data to quantify the error introduced in the identification process. The VFM is an inverse identification procedure based on the Principle of Virtual Works (PVW) [32; 7; 33; 34]. For small perturbations and under quasi-static loading, the PVW can be expressed as :

$$\underbrace{-\int_V \bar{\sigma}\left(X,\bar{\varepsilon}\right):\bar{\varepsilon}^*\,dV}_{W^*_{int}} + \underbrace{\int_{S_f}\vec{T}.\vec{u}^*\,dS_f}_{W^*_{ext}} = 0 \tag{9}$$

where V denotes the considered volume, $\bar{\sigma}$ the Cauchy stress tensor that depends on the constitutive set of parameters, X, and the strain field $\bar{\varepsilon}$. $\vec{u}^*$ and $\bar{\varepsilon}^*$ are the virtual displacement field and the associated virtual strain field, respectively. The external loads applied to surface S_f are denoted $\vec{T}$. To compute the internal virtual work, W^*_{int}, the integral is approximated by a discrete sum of all elementary volumes associated with data on pixels provided by the full-field measurements over the ROI. The stress tensor is computed with a *Z-mat* routine using the same algorithm as the FE simulations with *Z-set*. The expression of the external virtual work, W^*_{ext}, can be simplified by selecting a virtual displacement which is constant over the surface S_f, and equals $u^*_{S_f}$. In this case, W^*_{ext} is simply $u^*_{S_f}F$, where F is the resultant force measured with a load cell during the test.

The identification procedure with the VFM involves minimizing a cost function expressing the gap from PVW (simply the gap between W^*_{int} and W^*_{ext} in this case) for a given set of material parameters, X. The definition of the Virtual Fields (VF) therefore has a strong influence on identification results. Indeed, the choice of VF governs the implication of one or more components of the stress tensor in the PVW and thus in the identification problem. If several VF are defined, all associated expressions of the PVW are taken into account in the identification procedure. When identifying anisotropic plasticity, it is essential for all stress tensor components to be involved in the cost function, thus involving as many parameters as possible.

However, the definition of the optimal VF is an open problem [35]. In this study, three VF were defined empirically following the work of Rossi et al [11]. They are given in equation (10-12).

$$\vec{u}^{*(1)} = \begin{cases} 0 \\ \frac{y}{H} \end{cases} \quad \bar{\varepsilon}^{*(1)} = \begin{cases} 0 \\ \frac{1}{H} \\ 0 \end{cases} \tag{10}$$

$$\vec{u}^{*(2)} = \begin{cases} \frac{x}{W}\frac{(|y|-H)}{H} \\ 0 \end{cases} \quad \bar{\varepsilon}^{*(2)} = \begin{cases} \frac{(|y|-H)}{WH} \\ 0 \\ \mathrm{sgn}(y)\frac{x}{WH} \end{cases} \tag{11}$$

$$\vec{u}^{*(3)} = \begin{cases} \frac{1}{\pi}\sin\left(\pi\frac{x}{W}\right)\cos\left(\pi\frac{y}{2H}\right) \\ \frac{1}{\pi}\sin\left(\pi\frac{x}{W}\right)\cos\left(\pi\frac{y}{2H}\right) \end{cases} \quad \bar{\varepsilon}^{*(3)} = \begin{cases} \frac{1}{W}\cos\left(\pi\frac{x}{W}\right)\cos\left(\pi\frac{y}{2H}\right) \\ -\frac{1}{2H}\sin\left(\pi\frac{x}{W}\right)\sin\left(\pi\frac{y}{2H}\right) \\ \frac{1}{2}\left(\frac{1}{W}\cos\left(\pi\frac{x}{W}\right)\cos\left(\pi\frac{y}{2H}\right) - \frac{1}{2H}\sin\left(\pi\frac{x}{W}\right)\sin\left(\pi\frac{y}{2H}\right)\right) \end{cases} \tag{12}$$

where H and W are the half-height and half-width of the ROI considering that the geometry is centered with respect to the ROI. Only the first VF includes the external forces in the PVW and the others cancel it because $\vec{u}^{*(2)}$ and $\vec{u}^{*(3)}$ are equal to zero over the force application edges.

As stated before, a cost function deviation from the equilibrium for the PVW for each VF, N_{VF}, is expressed. In this study, the cost function, $\Phi(X)$, is written as the sum over the time steps, N_t, of the squared difference between the internal and the external virtual works (Eq. 13). The internal virtual work is approximated by a discrete sum of the data associated with the DIC measurement, N_{pt}. In order to compare the PVW between specimens, the cost function is normalized by the maximum value of the external virtual work over time obtained for the first VF.

Due to the large number of material parameters involved, the exploration of the cost function in the parameter ranges is complex. Moreover, as the reference material parameters are used in the FE simulations,

the PVW should be respected and the value of the cost function for reference parameters should be zero. So, the magnitude of the cost function stands for the error introduced in the identification procedure by the DIC and data processing. The quantification of this error is used as a second indicator in the present work to rank geometries for the identification of anisotropic material behaviour.

$$\Phi(X) = \frac{\sum_{i}^{N_{VF}} \sum_{t}^{N_t} \left[u_{S_f}^{*(i)}(t) F(t) - \sum_{j}^{N_{pt}} \bar{\sigma}_j \left(X,t\right) : \bar{\varepsilon}_j^{*(i)}(t) \right]^2}{\max_{N_t} \left[u_{S_f}^{*(1)}(t) F(t) \right]^2} \tag{13}$$

3 Specimen geometry ranking

In this second part of the paper, the tools and methods presented in the first part will now be implemented and the results discussed.

3.1 FE results

Non-biased reference data were obtained with FE simulations for the four geometries described previously. The equivalent plastic strain field and associated stress states projected onto the yield surface are shown in Figure 9 for the final step of the simulations as this is when most of the elements have reached plasticity. With the NOTCHED specimen (Figure 9-(a)), plasticity covers a large part of the ROI but the stress states remain close to uniaxial tension. On the contrary, the OPTIMIZED specimen exhibits localized plastic strain in small areas that cover only a few parts of the ROI (Figure 9-(d)). However, the stress states generated cover almost the entire yield surface, indicating high heterogeneity of stress fields and triaxiality ratio. The Σ and the D specimens were able to generate compression, uniaxial tension and shear stress states over a wide area of the ROI, but to a lesser extent than the OPTIMIZED specimen (Figures 9-(b) and (c)). In summary, these results confirm that the OPTIMIZED specimen generates a more heterogeneous stress field than the Σ and the D specimens. Moreover, the NOTCHED specimen generates the least heterogeneous stress field of the four specimens studied.

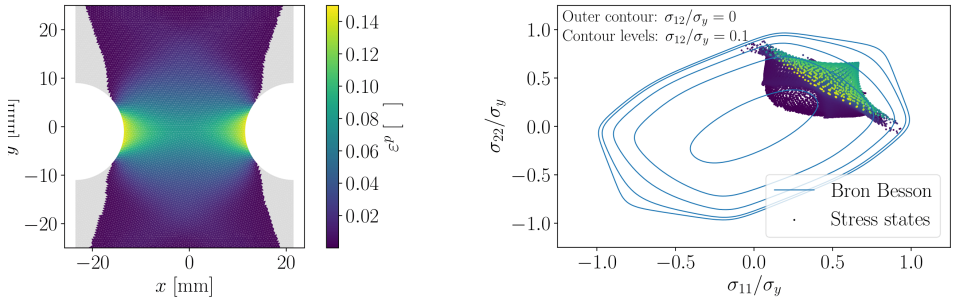

(a) - NOTCHED

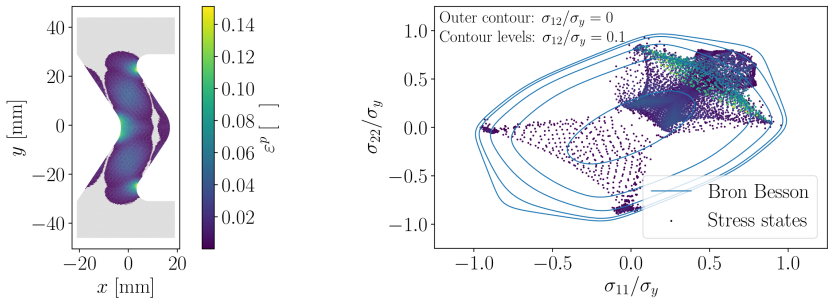

(b) - Σ

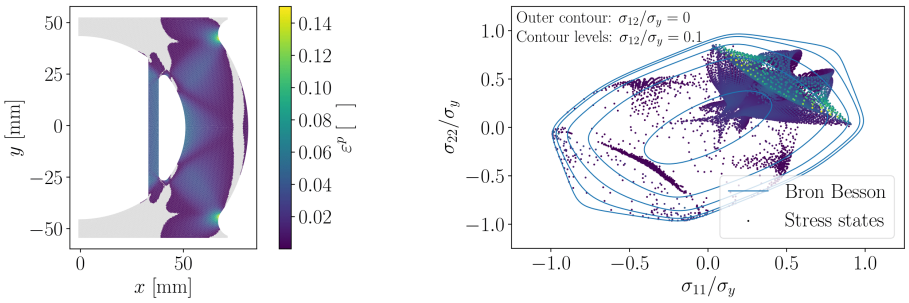

(c) - D

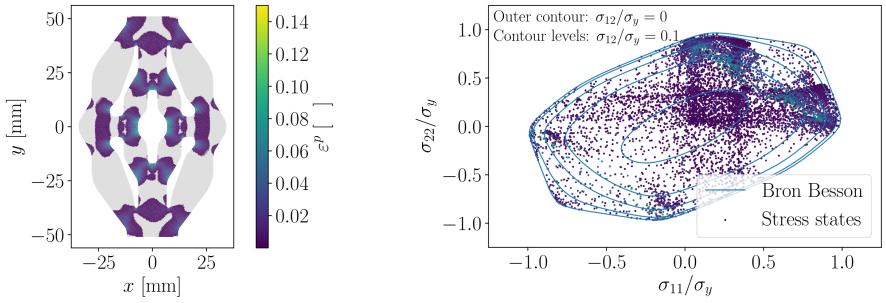

(d) - OPTIMIZED

Figure 9: Equivalent plastic strain field (light grey : $\varepsilon^p = 0$) and generated stress states projected onto the yield surface (unbiased data from FE)

3.2 Ranking by stress field heterogeneity using reference FE data

The heterogeneity indicator (Eq. 5) is used to quantify the level of heterogeneity and rank the specimens. Figure 10 shows each term used to compute the final value of the indicator. Their values agree with the previous analyses obtained with FE results. Indeed, the NOTCHED specimen (*i.e.*, the specimen with the lowest stress heterogeneity) has the lowest values of $\mathrm{Std}\,(TF)$ and $(TF)_R$; thus, leading to the lowest indicator value. However, the NOTCHED specimen has a high $\mathrm{Std}\,(\varepsilon^p)$ and $\mathrm{Av}_{\varepsilon^p}$ because the equivalent plastic strain is more widely spread over the ROI. The OPTIMIZED specimen has the highest ranking, the Σ and the D specimens (empirically designed) have equivalent rankings (about 0.25) and the NOTCHED specimen has the lowest ranking. As expected, based only on I_T, the OPTIMIZED specimen appears to be the most suitable for this identification problem, even if the $\mathrm{Std}\,(\varepsilon^p)$ was lowest for this specimen based on unbiased data from FE simulations.

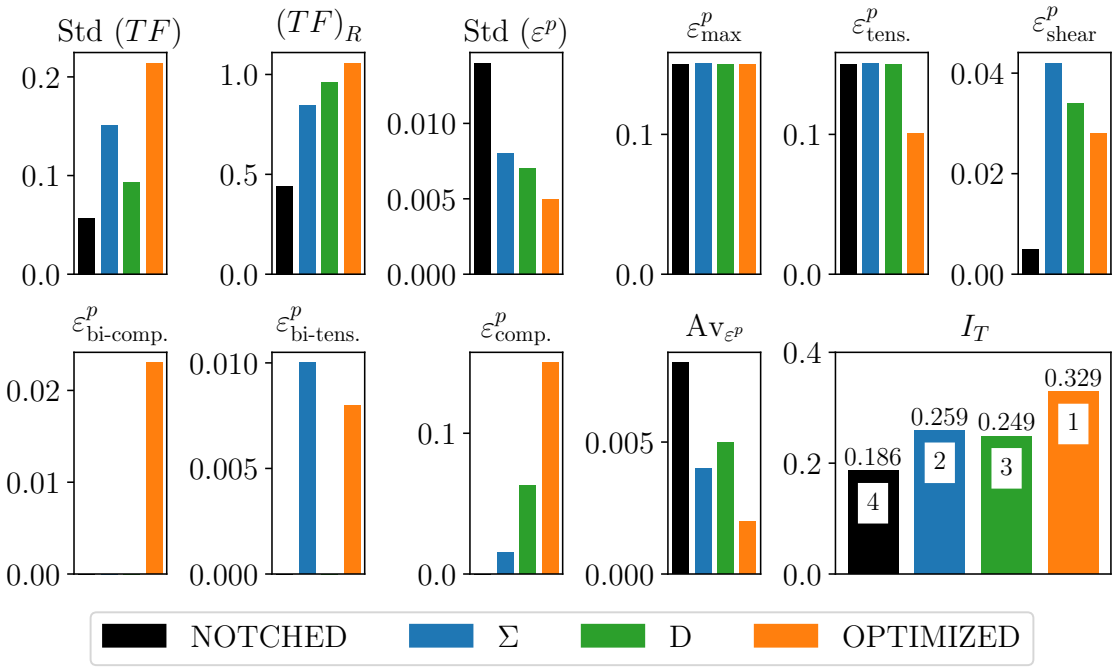

Figure 10: Values of the heterogeneity indicator and the constitutive terms

3.3 Effects of measuring and processing biases

This section studies the influence of experimental biases. The approach is based on synthetic test images processed using the DIC method to analyse the kinematic fields over the ROI. In this section, only speckle pattern N°1 is used (speckle pattern N°2 is used in section 3.5). Five configurations are compared in order to analyse the influence of each step of the process. For the following comparisons, the FE results are the reference data, *i.e.*, non-biased. The FE results were interpolated to the pixels and the data close to the

edges was reconstructed to analyse the influence of the reconstruction process. This configuration is named: "FE interpolated + edge reconstruction". For the following configurations, the data close to the edges were systematically reconstructed. The configuration named "DIC noise free images", refer to raw DIC results where every synthetic image was constructed using the same texture image. On the other hand, the "DIC noisy images" referred to raw DIC results where the sensor noise was taken into account by generating each synthetic image from a different texture image. The results from this last configuration were then smoothed to obtain the final configuration named "DIC noisy images smoothed". As an example, Figure 11 shows the strain in the loading direction (ε_{yy}) plotted along the minimum section of the NOTCHED specimen. As expected, reconstructing data at the edges by extending the last accurate value was the major source of errors (Figure 12). On the other hand, smoothing was able to limit the noise introduced by the DIC process or by the sensor. With this last approach, the result tends reasonably towards the FE reference.

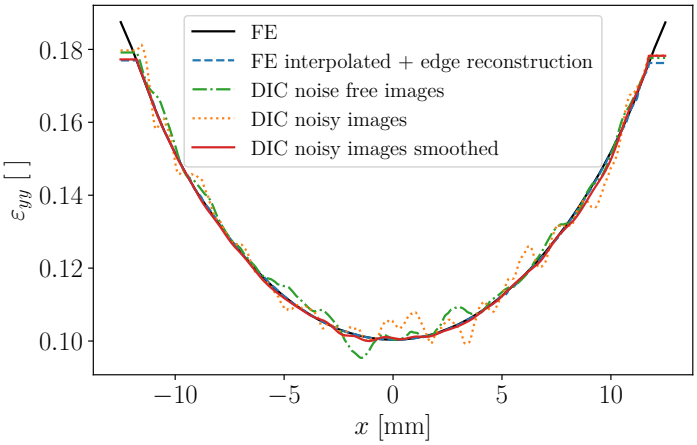

Figure 11: Variation in strain in the loading direction (ε_{yy}) in relation to the measurement process steps

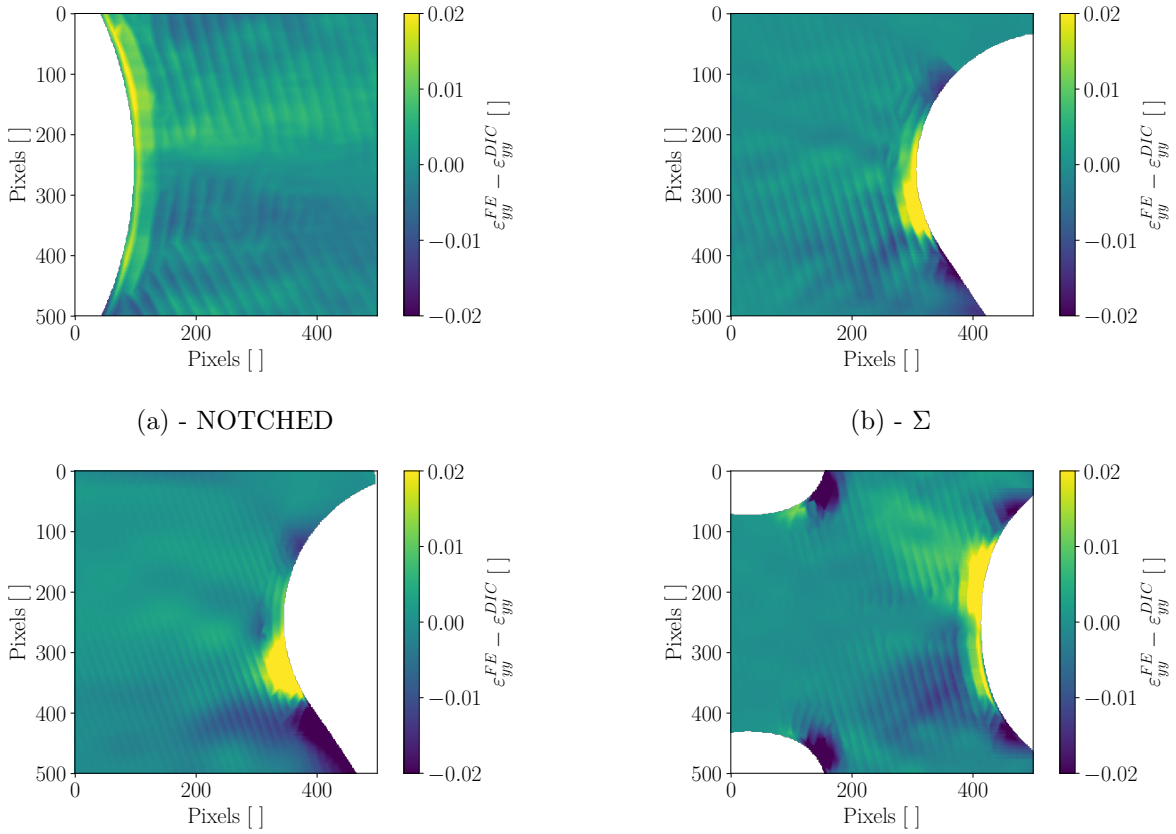

(a) - NOTCHED

(b) - Σ

(c) - D

(d) - OPTIMIZED

Figure 12: Difference between FE and smoothed DIC strain fields in the loading direction (ε_{yy}). The locations of the plotted areas are shown in Figure 3.

Figure 13 shows the influence of the measurement process on the equivalent plastic strain fields and the stress state range in comparison with the FE data in Figure 9. The surface of the specimen subjected to elastic strain is almost the same as FE results. However, plastic strain also appears in other locations due to noise and in particular close to the edges as expected by the observed difference between the reference strain and the computed strain (Figure 12). It is worth noting that the maximum value of plastic strain is reduced in all cases. On the other hand, the biases result in an artificial increase in the coverage of the yield surface for every specimen.

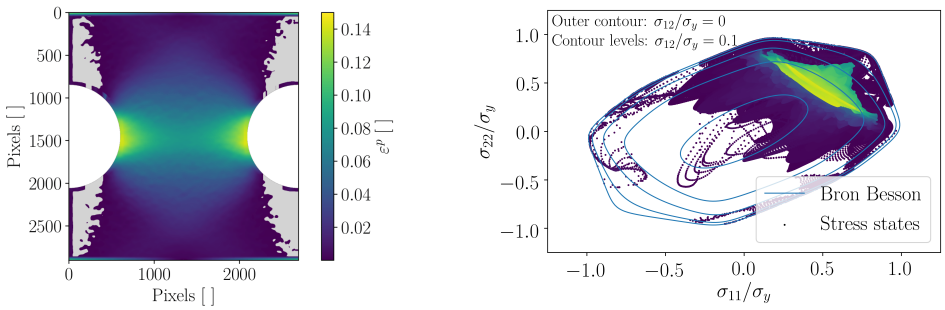

(a) - NOTCHED

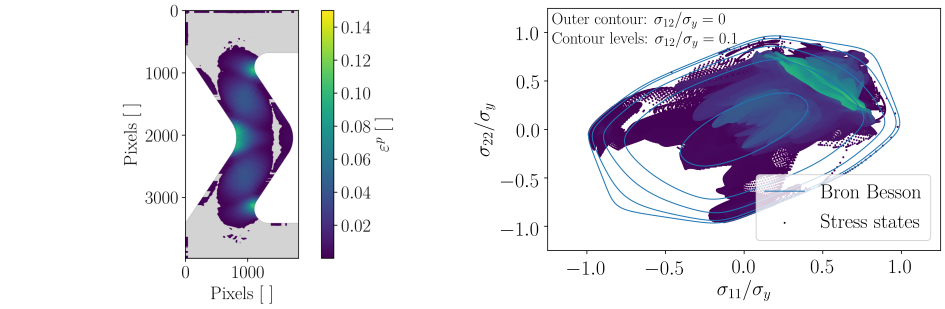

(b) - Σ

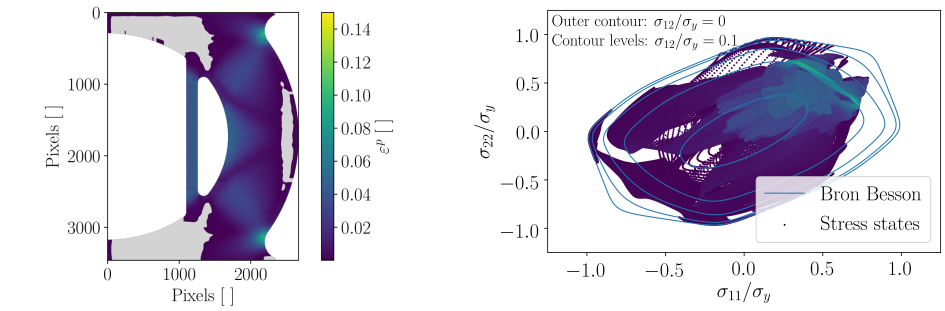

(c) - D

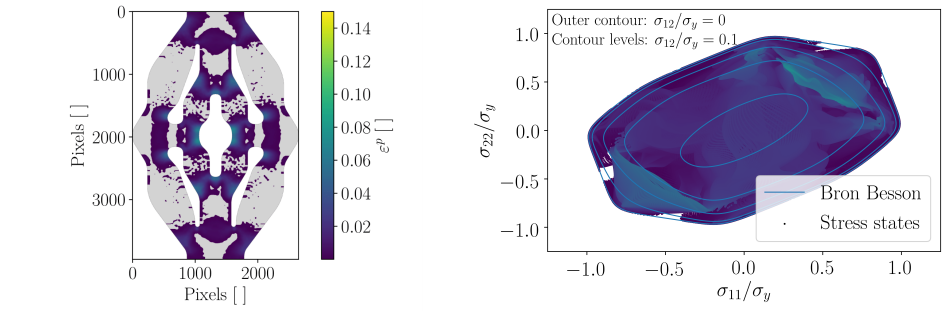

(d) - OPTIMIZED

Figure 13: Equivalent plastic strain field (light grey : $\varepsilon^p = 0$) and associated generated stress states projected onto the yield surface for DIC results obtained with smoothed strain fields.

These observations can be quantified by analysing the heterogeneity indicator obtained by taking into

account the measurement process (Fig. 14). First, the reconstruction of the edges decreased the value of the indicator because the maximum value of ε_p also decreased. The influence of this step was more significant for the OPTIMIZED specimen than for the NOTCHED one due to the high strain localisation. Secondly, the noise introduced by DIC and the sensor rises the value of I_T for every specimen because incorrect stress states appear. This overestimation is balanced by the smoothing of the fields. Finally, using biased data completely changes the heterogeneity indicator. The NOTCHED and the OPTIMIZED specimens converged to almost the same value while the influence of the measuring process has similarly lowered the value of I_T for the Σ and the D specimens.

From these results, one could consider the relative difference between the final (DIC noisy images smoothed) and reference (FE) I_T value as an indicator of the noise sensitivity. The values are $\Delta I_T/I_T^{FE} =$ 0.333, -0.174, -0.201 and -0.240 for the NOTCHED, the Σ, the D and the OPTIMIZED specimens respectively. This classification must be taken with caution. With this noisy data, it is not obvious that the specimen with the lowest $\Delta I_T/I_T^{FE}$ value is the one that allows a robust identification of the targeted parameters. This is why it is necessary to analyse the impact of measurement biases in the identification process.

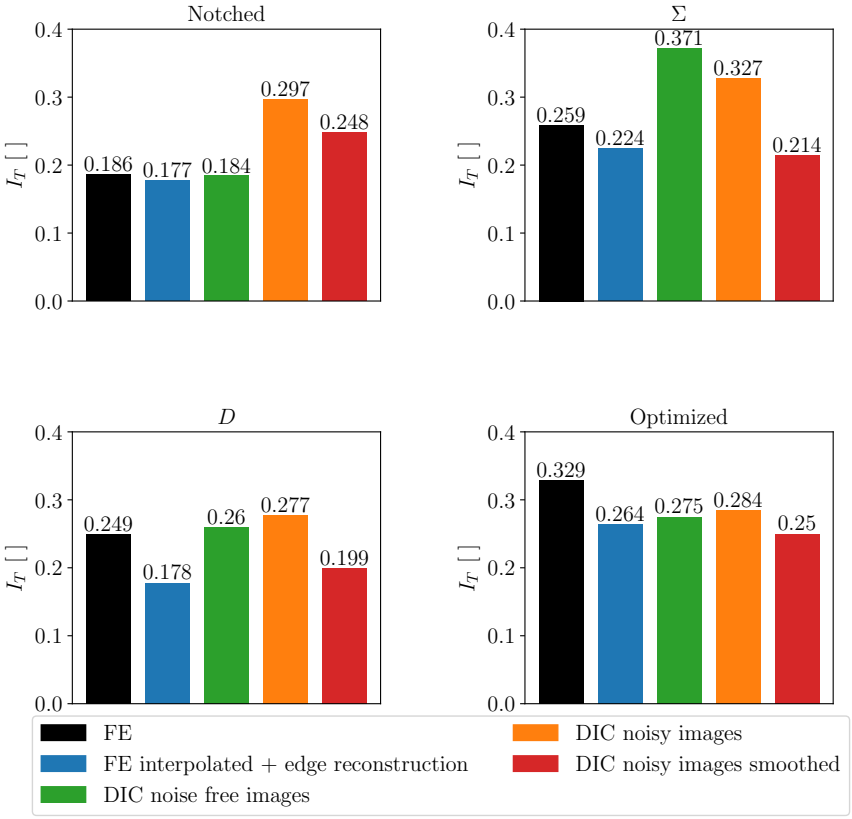

Figure 14: Values of I_T with bias data generated with the same set of images for every specimen

3.4 Ranking by error in the identification process

This section is about quantifying the error introduced in the identification process when running an alternative classification. With this aim, the cost functions obtained using the PVW (Eq. 13) with the VF (Eq. 10-12) were computed for the four specimens and for the five configurations presented previously. The magnitude of the error in the final cost function value that can be attributed to each of these virtual fields was computed and it was verified that their relative contribution was balanced. With unbiased data (FE), the cost functions are always very close to zero. Any deviation from PVW equilibrium can only be caused by the different steps in the measurement process, which can jeopardize the identification procedure.

Figure 15 gives the numerical value of the second indicator (VFM cost function) for each configurations related to the measurement process steps:

- reconstructing data close to the edge does not add a significant error while strong strain localization can be seen on the OPTIMIZED specimen, for example,

- using synthetic images to take the DIC biases into account increased the value of the indicator for all the specimens. The OPTIMIZED and the Σ specimens seems to be more sensitive to DIC biases,
- it could also be noted that the noise introduced by the sensor increases the value of the indicator regardless of the specimen. OPTIMIZED and Σ specimens are the most sensitive to camera sensor noise (DIC noisy images),
- smoothing the strain fields limits the effect of DIC biases on the identification procedure, for Σ and OPTIMIZED specimens in particular.

Using the final configuration data, another classification can be applied using the value of the second indicator. The simplest geometry (NOTCHED) is found to be the best in this case. The Σ and the D specimens have the highest indicator values, which reflect the high sensitivity of the identification procedure to measurement biases. It is worth noting that both specimens that were empirically designed have almost the same indicator value. However, their sensitivity to the different steps of the measurement process is different. Finally, the most complex specimen (OPTIMIZED) is ranked second. Finally, it can be concluded that the two selection criteria give different rankings for the specimens.

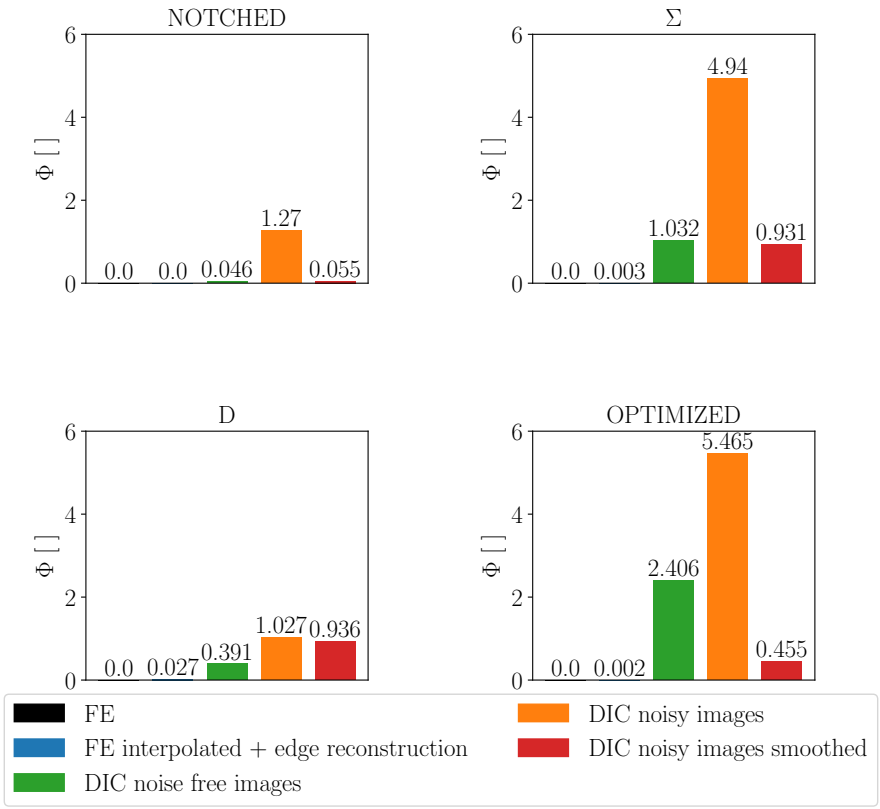

Figure 15: Second selection criterion (VFM cost function) value with biased data generated with the same set of images for every specimen

3.5 Robustness for the speckle pattern

To evaluate the dependency of the ranking based on the second criterion for the speckle pattern, a second set of synthetic images was generated using the images for speckle pattern N°2 as described in section 2.4. This speckle pattern results in a higher level of measurement noise (Figure 7).

Figure 16 compares the value of the second selection criterion for the two speckle patterns for each configuration. It can be seen that the rankings obtained for both speckle patterns are different. However, the NOTCHED specimen is still the most robust in terms of measurement biases for both speckle patterns. The D specimen exhibits a very similar trend for both speckle patterns, a lower indicator value is even obtained for the second speckle pattern. On the contrary, the Σ and OPTIMIZED specimens are more sensitive to noise when looking at the "DIC noisy images" in Figure 16. Again this dependency is reduced when smoothing the strain fields. However, this time the OPTIMIZED specimen has the highest value of the second

selection criterion.

Overall, ranking the specimens under the second selection criterion for the last configuration ("DIC noisy images smoothed") may not be sufficient when designing an optimized specimen. It would be worth ensuring that no large values are reached in previous configuration ("DIC noise free images" or "DIC noisy images") since it may highlight a strong sensitivity to measurement biases.

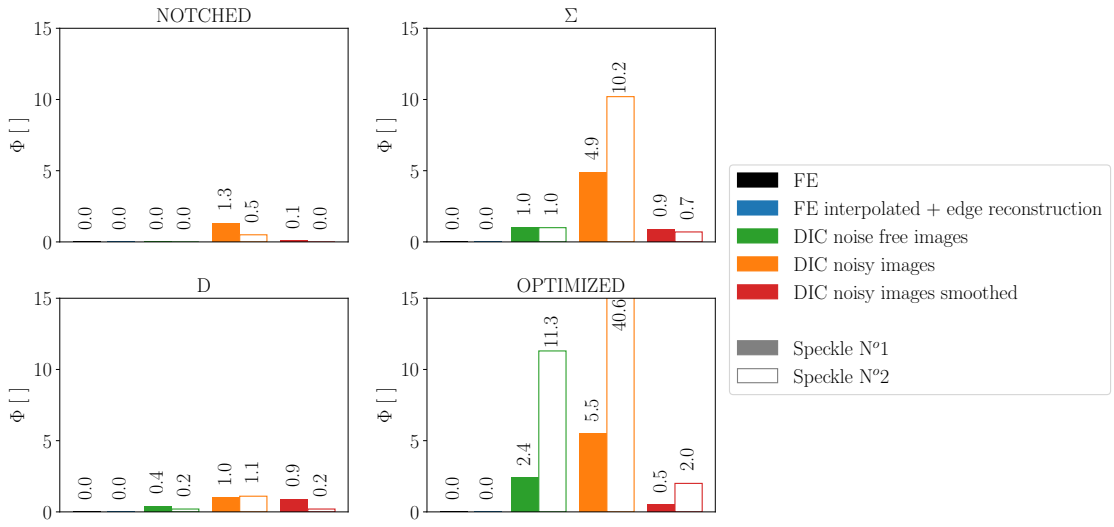

Figure 16: Second selection criterion (VFM cost function) values with biased data for the two speckles

4 Discussions

In this work two criteria were assessed. The first one was based on the stress states heterogeneity and the second one was based on errors introduced in the VFM identification. Both criteria lead to different ranking of specimens. Therefore, it would be challenging to define an enriched criterion based on a compromise between stress field heterogeneity and robustness. From this work results, and considering a specific setup (camera resolution, correlation software, ...), the D specimen seems to be the most promising.

The study demonstrated the dependence of the ranking on the speckle pattern used for DIC. Here, only two speckles patterns were considered. So, to be confident about the robustness of a specimen, a significant number of speckle patterns should be tested. An alternative could be to use an optimized speckle pattern [36] or measurement methods based on regular patterns [37; 38] that would ensure that the second selection criterion is not dependent on the speckle pattern.

Also, as it was defined in this study, the cost function value used to compute the second criterion quantifies the gap to mechanical equilibrium. Assuming that the global minimum of the cost function is reached, the identification of a suitable set of material parameters is guaranteed. However, it does not ensure the identifiability of each parameter independently. To analyse that point, the cost function sensitivity to each parameter could be computed with reference and biased data. Knowing that an unbalanced involvement of material parameters in mechanical response can jeopardize the identification of low-weight parameters, the criterion could be enriched by taking into account that possible unbalanced contribution to the cost-function, always with more or less biased data. Note that, together with the optimisation of the ranking criterion, further improvements could consist in the use of sensitivity virtual fields [39] to reach a more balanced involvement of all parameters.

5 Conclusions and future works

The paper deals with the robustness, in terms of measurement biases, of specimen design criteria used to identify anisotropic mechanical behaviour. Indeed, to the authors' knowledge, the specimen design is only assessed based on numerical simulations and does not take the effect of the biases from the full-field measurement method for mechanical fields into account. This work considers four specimens with increasing geometry complexity. Numerical simulations were run using the Finite Element method to generate a reference data set. Synthetic test images have been generated to study the influence of the measurement biases. These images were then processed using the Digital Image Correlation method to compute the kinematic fields for the specimens.

First, since various stress states are involved in the identification of an anisotropic yield criterion, a heterogeneity criterion based on unbiased reference data was computed to rank the four specimens. Then, a second criterion based on the Virtual Field Method has been computed to quantify the error introduced in the identification procedure by measurement biases. The current study led to the following conclusions:

- the first criterion was able to deliver the expected ranking of specimens regarding geometry complexity and design methods (from adding singularities to standard specimens for topological optimization),
- the second criterion can be used to identify the steps in the measurement process that imply greater error in the identification procedure. In the present work, the sensor noise or the DIC noise lead to

significant error,

- the simplest geometry (NOTCHED) is found to be the most robust in terms of measurement and process biases,
- the most complex geometry (OPTIMIZED) is found to be the most sensitive to DIC and sensor noise which could make it challenging in experimental conditions.

The perspective of this work is to perform experiments with each specimen. It will be very interesting to verify the consistency of the strain fields obtained by the DIC using synthetic images and those from experiments. Then, the ranking could be confirmed and the material parameters could be identified and compared to reference value obtained with uniaxial tensile tests.

Acknowledgement

The authors are grateful to ONERA and the Région Hauts-de-France for cofunding this project. Also, the authors would like to express their sincere gratitude to Constellium and more specifically to Dr. Jean-Christophe Ehrström for supporting this study by providing the tested aluminum sheet.

Data availability

The data that support the findings of this study are available from the corresponding author, upon reasonable request.

Appendix

DIC Hardware Parameters	NOTCHED	Σ	D	OPTIMIZED
Camera	Nikon D300 12M (4288x2848 px)			
Lens	Micro Nikkor 105mm			
FOV	48.5×47.9mm	87.5×40.0mm	106.9×82.5mm	102.0×68.3mm
Image Scale	0.0167 mm/pix 59.88 pix/mm	0.022 mm/pix 45.45 pix/mm	0.0309 mm/pix 32.36 pix/mm	0.0258 mm/pix 38.75 pix/mm
Image Acquisition Rate	1Hz			
Patterning Technique	Spray paint			

Table A1: DIC configuration

DIC analysis parameters	NOTCHED	Σ	D	OPTIMIZED
DIC software	FOLKI-D developed by ONERA			
Matching criterion	ZNCC			
Subset size radius	15pix	15pix	40pix	15pix
Step size	1 px			
Subset shape function	First order polynomial			
Strain formulation	Subset shape function			
Strain window radius	15pix	15pix	40pix	15pix
Spatial strain filtering	Gaussian window			
Standard deviation	15 pix	15pix	15pix	15pix
Temporal strain filtering	Gaussian window			
Standard deviation	5 time steps	5 time steps	5 time steps	5 time steps
Edge reconstruction	40 pix	20 pix	40 pix	30 pix

Table A2: DIC configuration with speckle pattern N°1

DIC Analysis Parameters	NOTCHED	Σ	D	OPTIMIZED
DIC software	FOLKI-D developed by ONERA			
Matching criterion	ZNCC			
Subset size radius	20pix	10pix	40pix	10pix
Step size	1 px			
Subset shape function	First order polynomial			
Strain formulation	Subset shape function			
Strain window radius	40pix	15pix	20pix	10pix
Spatial strain filtering	Gaussian window			
Standard deviation	15 pix	15pix	20pix	15pix
Temporal strain filtering	Gaussian window			
Standard deviation	3 time steps	5 time steps	7 time steps	7 time steps
Edge reconstruction	40 pix	40 pix	40 pix	30 pix

Table A3: DIC configuration with speckle pattern N°2

References

[1] Jianqiang Chen, Yazid Madi, Thilo F. Morgeneyer, and Jacques Besson. Plastic flow and ductile rupture of a 2198 Al–Cu–Li aluminum alloy. *Computational Materials Science*, 50(4):1365 – 1371, 2011.

[2] F. Barlat, J. C. Brem, J. W. Yoon, K. Chung, R. E. Dick, D. J. Lege, F. Pourboghrat, S.-H. Choi, and E. Chu. Plane stress yield function for aluminum alloy sheets—part 1: theory. *International Journal of Plasticity*, 19(9):1297 – 1319, 2003.

[3] F. Bron and J. Besson. A yield function for anisotropic materials. Application to aluminum alloys. *International Journal of Plasticity*, 20(4):937 – 963, 2004.

[4] F. Barlat and K. Lian. Plastic behavior and stretchability of sheet metals. Part I: A yield function for orthotropic sheets under plane stress conditions. *International Journal of Plasticity*, 5(1):51 – 66, 1989.

[5] F. Barlat, H. Aretz, J. W. Yoon, M. E. Karabin, J. C. Brem, and R. E. Dick. Linear transformation-based anisotropic yield functions. *International Journal of Plasticity*, 21(5):1009 – 1039, 2005.

[6] Michel Grédiac and François Hild. *Full-Field Measurements and Identification in Solid Mechanics*. December 2012.

[7] Stéphane Avril, Marc Bonnet, Anne-Sophie Bretelle, Michel Grédiac, François Hild, Patrick Ienny, Félix Latourte, Didier Lemosse, Stéphane Pagano, Emmanuel Pagnacco, and Fabrice Pierron. Overview of Identification Methods of Mechanical Parameters Based on Full-field Measurements. *Experimental Mechanics*, 48(4):381–402, 2008.

[8] Stéphane Roux and François Hild. Optimal procedure for the identification of constitutive parameters from experimentally measured displacement fields. *International Journal of Solids and Structures*, 2018.

[9] F. Pierron and M. Grédiac. Towards Material Testing 2.0. A review of test design for identification of constitutive parameters from full-field measurements. *Strain*, 57(1):e12370, 2021. _eprint: https://onlinelibrary.wiley.com/doi/pdf/10.1111/str.12370.

[10] M. H. H. Meuwissen, C. W. J. Oomens, F. P. T. Baaijens, R. Petterson, and J. D. Janssen. Determination of the elasto-plastic properties of aluminium using a mixed numerical–experimental method. *Journal of Materials Processing Technology*, 75(1):204 – 211, 1998.

[11] Marco Rossi, Fabrice Pierron, and Michaela Štamborská. Application of the virtual fields method to large strain anisotropic plasticity. *International Journal of Solids and Structures*, 97-98:322–335, October 2016.

[12] J.-H. Kim, F. Barlat, F. Pierron, and M.-G. Lee. Determination of Anisotropic Plastic Constitutive Parameters Using the Virtual Fields Method. *Experimental Mechanics*, 54(7):1189–1204, September 2014.

[13] A. Khalfallah, H. Bel Hadj Salah, and A. Dogui. Anisotropic parameter identification using inhomogeneous tensile test. *European Journal of Mechanics - A/Solids*, 21(6):927 – 942, 2002.

[14] José Aquino, A. Gil Andrade-Campos, João M. P. Martins, and Sandrine Thuillier. Design of heterogeneous mechanical tests: Numerical methodology and experimental validation. *Strain*, 55:e12313, 2019.

[15] S. Cooreman, D. Lecompte, H. Sol, J. Vantomme, and D. Debruyne. Identification of Mechanical Material Behavior Through Inverse Modeling and DIC. *Experimental Mechanics*, 48(4):421–433, August 2008.

[16] S. Schmaltz and K. Willner. Comparison of Different Biaxial Tests for the Inverse Identification of Sheet Steel Material Parameters. *Strain*, 50(5):389–403, 2014.

[17] J. M. P. Martins, A. Andrade-Campos, and S. Thuillier. Calibration of anisotropic plasticity models using a biaxial test and the virtual fields method. *International Journal of Solids and Structures*, 2019.

[18] T. Pottier, F. Toussaint, and P. Vacher. Contribution of heterogeneous strain field measurements and boundary conditions modelling in inverse identification of material parameters. *European Journal of Mechanics - A/Solids*, 30(3):373 – 382, 2011.

[19] E. M. C. Jones, J. D. Carroll, K. N. Karlson, S. L. B. Kramer, R. B. Lehoucq, P. L. Reu, and D. Z. Turner. Parameter covariance and non-uniqueness in material model calibration using the Virtual Fields Method. *Computational Materials Science*, 152:268–290, September 2018.

[20] N. Souto, A. Andrade-Campos, and S. Thuillier. A numerical methodology to design heterogeneous mechanical tests. *International Journal of Mechanical Sciences*, 107:264 – 276, 2016.

[21] Yi Zhang, Sam Coppieters, Sanjay Gothivarekar, Arne Van de Velde, and Dimitri Debruyne. Independent Validation of Generic Specimen Design for Inverse Identification of Plastic Anisotropy, April 2021. Publisher: Prof. Anne Marie Habraken.

[22] Mariana Conde, António Andrade-Campos, Miguel Guimarães Oliveira, and João Miguel Peixoto Martins. Design of heterogeneous interior notched specimens for material mechanical characterization, March 2021. Publisher: Prof. Anne Marie Habraken.

[23] B. Barroqueiro, A. Andrade-Campos, João Dias-de Oliveira, and R. A. F. Valente. Design of mechanical heterogeneous specimens using topology optimization. *International Journal of Mechanical Sciences*, page 105764, May 2020.

[24] Filipe Almeida, Bruno Barroqueiro, João Dias-de Oliveira, and António Gil Andrade-Campos. On the Development of a Heterogeneous Mechanical Test Specimen Using Topology Optimization. *Procedia Manufacturing*, 47:816–823, January 2020.

[25] Miguel G Oliveira, Sandrine Thuillier, and António Andrade-Campos. Evaluation of heterogeneous mechanical tests for model calibration of sheet metals. *The Journal of Strain Analysis for Engineering Design*, page 03093247211027061, July 2021. Publisher: IMECHE.

[26] N. Souto, S. Thuillier, and A. Andrade-Campos. Design of an indicator to characterize and classify mechanical tests for sheet metals. *International Journal of Mechanical Sciences*, 101-102:252 – 271, 2015.

[27] Pascal Bouda, Bertrand Langrand, Delphine Notta-Cuvier, Eric Markiewicz, and Fabrice Pierron. A computational approach to design new tests for viscoplasticity characterization at high strain-rates. *Computational Mechanics*, June 2019.

[28] W. F. Hosford. A Generalized Isotropic Yield Criterion. *Journal of Applied Mechanics*, 39(2):607–609, 1972.

[29] Jean-Didier Garaud, Johann Rannou, Christophe Bovet, Sylvia Feld-Payet, Vincent Chiaruttini, Basile Marchand, Laurent Lacourt, V A Yastrebov, Nicolay Osipov, and Stéphane Quilici. Z-set -suite logicielle pour la simulation des matériaux et structures. In *14ème Colloque National en Calcul des Structures*, Presqu'île de Giens (Var), France, May 2019.

[30] G. Le Besnerais, Y. Le Sant, and D. Lévêque. Fast and Dense 2D and 3D Displacement Field Estimation by a Highly Parallel Image Correlation Algorithm. *Strain*, 52(4):286–306, 2016. _eprint: https://onlinelibrary.wiley.com/doi/pdf/10.1111/str.12194.

[31] A Good Practices Guide for Digital Image Correlation, 2018.

[32] M. Grédiac, F. Pierron, S. Avril, and E. Toussaint. The Virtual Fields Method for Extracting Constitutive Parameters From Full-Field Measurements: a Review. *Strain*, 42(4):233–253, 2006.

[33] F. Pierron and M. Grediac. *The virtual fields method: Extracting constitutive mechanical parameters from full-field deformation measurements*. Springer New York, 2012.

[34] Eric Markiewicz, Bertrand Langrand, and Delphine Notta-Cuvier. A review of characterisation and parameters identification of materials constitutive and damage models: From normalised direct approach to most advanced inverse problem resolution. *International Journal of Impact Engineering*, 110:pages 371 – 381, 2017. Publisher: Elsevier.

[35] Aleksander Marek, Frances M. Davis, and Fabrice Pierron. Sensitivity-based virtual fields for the non-linear virtual fields method. *Computational Mechanics*, 60(3):409–431, September 2017.

[36] Sven Bossuyt. Optimized Patterns for Digital Image Correlation. In Helena Jin, Cesar Sciammarella, Cosme Furlong, and Sanichiro Yoshida, editors, *Imaging Methods for Novel Materials and Challenging Applications, Volume 3*, Conference Proceedings of the Society for Experimental Mechanics Series, pages 239–248, New York, NY, 2013. Springer.

[37] Yves Surrel. Moire and grid methods: a signal-processing approach. In *Interferometry '94: Photomechanics*, volume 2342, pages 118–127. International Society for Optics and Photonics, November 1994.

[38] M. Grédiac, F. Sur, and B. Blaysat. The Grid Method for In-plane Displacement and Strain Measurement: A Review and Analysis. *Strain*, 52(3):205–243, 2016.

[39] Aleksander Marek, Frances M. Davis, Marco Rossi, and Fabrice Pierron. Extension of the sensitivity-based virtual fields to large deformation anisotropic plasticity. *International Journal of Material Forming*, July 2018.